Sustainable low temperature preparation of Mn3–xCoxO4 ($0 \leq x < 3$) spinel oxide colloidal dispersions used for solar absorber thin films

Guillaume Salek, Pascal Dufour, Sophie Guillemet-Fritsch, Christophe Tenailleau

http://dx.doi.org/10.1016/j.matchemphys.2015.05.065

Sustainable low temperature preparation of $Mn_{3-x}Co_xO_4$ ($0 \leq x < 3$) spinel oxide colloidal dispersions used for solar absorber thin films

G. Salek, P. Dufour, S. Guillemet-Fritsch, C. Tenailleau*

Centre Interuniversitaire de Recherche et d'Ingénierie des MATériaux (CIRIMAT), UMR CNRS 5085, Université de Toulouse – UPS, 118 Route de Narbonne, 31062 Toulouse Cedex 09, France

HIGHLIGHTS

- Sustainable low temperature synthesis of oxide nanoparticles.
- Stabilization of colloidal dispersions free of organic precursors or surfactants.
- Influence of hydrodynamic parameters and physicochemical properties.
- Thin films preparation by the dip-coating method and their optical properties.
- Promising method for enhanced efficiency in the preparation and use of nanomaterials.

GRAPHICAL ABSTRACT

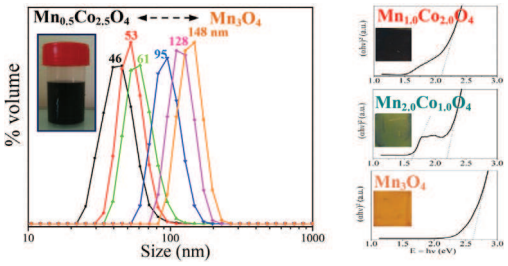

ABSTRACT

The preparation of pure crystalline oxide nanoparticles (with controlled composition, size and shape) and formation of stable suspensions free of complex organic precursors was developed and optimized at room temperature (or below 100 °C). This reproducible water and ethanol synthesis and solution stabilization of oxide nanoparticles is based on $Mn_{3-x}Co_xO_4$ ($0 \leq x < 3$) composition materials. To our knowledge, this is the first study on the complete Mn–Co–O spinel system synthesized at low temperature. The main hydrodynamic parameters, as well as the physical and chemical properties that control the oxide precipitation and nanoparticle size and morphology were characterized in detail for the family end member Mn_3O_4 and used for the other compositions. X-ray diffraction and Scanning Electron Microscopy images showed the influence of the alkaline solution concentration, pH, temperature and solvent on the nanoparticles properties. Neutron diffraction was used for determining the cationic distribution in two compositions, i.e. $CoMn_2O_4$ and $MnCo_2O_4$. While the tetrahedral site is mainly occupied by Co^{2+}, four types of cations were determined for the octahedral sites. Zeta potential and rheological measurements were performed to determine the stability region of nanoparticles in aqueous solution. This innovative and low cost process was used to produce homogenous and crystalline metal oxide thin films that can be used as solar absorbers in various applications. Their optical properties were characterized. A second absorption edge, due to cobalt and observed in the visible region, is attributed to an intermediate band gap, which is a very important feature, especially for future solar cells. This sustainable synthesis of oxide nanoparticles and thin film preparation procedure is applicable to other oxide families.

Keywords:
Oxides
Precipitation
Thin films
Optical properties

* Corresponding author.
E-mail address: tenailleau@chimie.ups-tlse.fr (C. Tenailleau).

1. Introduction

Light absorber materials are the key components of systems that are capable of transforming solar energy into an useful energy for our modern needs. Photosynthesis, photochemistry, photocatalysis and photovoltaics are important research areas that study the interaction of light within a system in the aim of activating chemical reactions and/or producing electricity. Transition metal oxides, which crystallize with the spinel structure, are among the different families of light absorber materials. These have always been considered with a great attention thanks to their very interesting optical, electrical and magnetic properties related to the multi-valence cation. During the last decades, these were largely studied for various types of applications including photothermal conversion [1,2], pigments for paints [3,4], thermistors [5,6] catalysis [7] etc … Moreover, transition metals are naturally abundant and transition metal oxides are usually chemically stable with no adverse effect on the environment.

The initial motivation of this work was to produce homogenous and crystalline metal oxide thin films by a simple process that can be used as solar absorbers in solar cells. In particular, oxide thin films of spinel type can be incorporated in all-oxide photovoltaic cells, a new field in photovoltaics as evidenced by Rühle et al., in 2012 [8]. Most of the components of optoelectronic systems should have no toxicity, improved capabilities and favor miniaturization. Thin layers of nanomaterials can be prepared by different techniques: physical vapor deposition [9,10], chemical vapor deposition [11,12], serigraphy or electrochemistry [13,14], but most of them remain complicated or expensive to use. Tape casting, spin-coating and dip-coating are now very well developed techniques which enable the preparation of homogenous thin films that can be extended to a larger scale at low costs. These techniques require stable solutions of precursors. Nowadays, the sol–gel method is the most frequent process used for the elaboration of coatings at low temperature [15–17]. However, this method usually implies the use of non-environmentally friendly complex organic agents and surfactants. Their removal also generally implies thermal decomposition which can strongly deteriorate the thin films.

We developed a simple synthetic approach for preparing crystallized nanoparticles of solar light absorber oxides at room temperature by inorganic polycondensation, mainly in water. The main parameters responsible for the spinel oxide nanoparticle crystallization in solution with controlled shape and size were studied in detail for the end member Mn_3O_4 of the spinel Mn–Co–O family. A meticulous work based on the understanding and control of the physical and chemical properties of particles in aqueous solution allowed us to extend the synthesis to the whole range of compositions $Mn_{3-x}Co_xO_4$ ($0 < x < 3$) and to obtain a full set of pure manganese and cobalt spinel oxide stabilized sols. Oxide thin films were then prepared at ambient atmosphere by the dip-coating method and their optical properties studied over the UV–Vis-IR regions.

2. Materials and methods

2.1. Preparations of oxide nanoparticles, colloidal dispersions and thin films

The precipitation method, which consists of mixing an aqueous solution of metal salts with an alkaline solution, is a simple, robust and low cost method. The condensation of cations in solution, depending on their nature and valence, as well as the aqueous medium conditions (Temperature and pH, essentially) can lead to the formation of oxide particles with tailored size and morphology that are directly crystallized in solution. Under our standard synthesis conditions, a volume of 100 mL of metal sulfate salt precursors (99% $MnSO_4 \cdot H_2O$ and 98% $CoSO_4.7H_2O$ from Alfa Aesar) with a concentration of 0.3 mol L^{-1} were quickly introduced in the middle of a dilute alkaline solution containing 66% molar excess of $LiOH \cdot H_2O$ (>99% purity, purchased from Sigma) dissolved in 1400 mL of water ($C = 0.045$ mol L^{-1}) to obtain complete precipitation and to ensure a strong alkaline solution. A constant stirring (300 rpm) was maintained during stirring for 30 min. Then three successive steps of centrifugation at 4000 rpm and washings with water were used for removing residual ions (Li^+ and SO_4^{2-}). The supernatant conductivity, initially at 8 mS cm^{-1}, decreases by 10^3 magnitudes of order after washings, close to the value of pure distilled water (5 μS cm^{-1}).

A peptization stage at pH = 6 with nitric acid (10^{-6} M) was then applied in order to stabilize colloidal suspensions of our spinel oxide nanoparticles. Again, three successive steps of centrifugation (8000 rpm) and washings here with absolute ethanol for a total volume of ~20 mL were performed. Finally, oxide nanoparticles were dispersed in an azeotrope solution containing 96% of absolute ethanol mixed with ultrapure water and sonicated at a frequency of 35 kHz for 5 min. The azeotrope solution can ensure a constant concentration of solvent during evaporation and the dielectric constant here obtained can improve the wettability of the suspension onto the substrate.

Oxide thin films were prepared at ambient pressure by the dip-coating technique using the previously made colloidal dispersion with a dip and retrieval speed of 200 mm min^{-1} and the substrate was immerged for 30 s. Commercial sodo-calcic glasses (5 mm in thickness) were used as substrates for spinel oxide optical properties measurements.

2.2. Characterizations

Crystalline state and phase purity of the spinel oxides were characterized by X-ray diffraction (XRD) at room temperature with a Bruker D4 ENDEAVOR diffractometer using CuKα radiation (40 kV, 40 mA).

Scanning Electron Microscopy (SEM) images used for determining particles morphology and size, and for thin film surface were obtained with a JEOL JSM 6700F Microscope equipped with a Field Emission Gun.

Chemical analyses of the elements Mn, Co, Li and S were realized by Induced Coupled Plasma and Atomic Emission Spectrometry (ICP-AES) using a Jobin-Yvon 2000 instrument.

Neutron diffraction data were collected at room temperature on the Super D2B instrument available at the Institut Laue Langevin (ILL), Grenoble, France, in order to determine the cation distribution. Around 3 g of sample powders were inserted into vanadium cylinders for measurements. Only two spinel oxides ($CoMn_2O_4$ and $MnCo_2O_4$) could be run through the easy access process available at the ILL. The Super D2B instrument has a 135° take-off angle and 128 ^{3}He detectors. Powder diffraction patterns were recorded using a 1.5941 Å wavelength in the 10–160° 2θ range with a 0.05° step and a scan of 500,000 counts. All neutron data were analyzed for structural determination using the Rietveld method compiled with the FULLPROF program [18]. Typical structural parameters were refined, in order: scale factor, first terms of the background, zero shift, cell parameters, peak shape factors, atomic positions, thermal factors, absorption coefficient and site occupancies. Bond valence sum (BVS) calculations were also performed using the neutron data and the FULLPROF program considering two cations (Co^{2+} and Mn^{2+}) for the tetrahedral sites and four cations (Co^{2+}, Co^{3+}, Mn^{3+} and Mn^{4+}) for the octahedral sites based on previous results [19,20]. The cation concentrations on the octahedral site were calculated by determining the individual bond valence sums

obtained for two cations of a same element, which were averaged to the equivalent charge of the element.

Zeta Potential measurements were performed with a Zetasizer 3000 Malvern Instrument at a wavelength of 633 nm in order to determine the best pH areas for preparing colloidal suspensions. First, each oxide solution containing anionic flocculates was dispersed in distilled water to obtain a 0.001 volume fraction of particles. Each solution was then divided into ten equivalent parts that were studied under various pH conditions. Half were diluted with different quantities of 1 M nitric acid (pH < 7) and the other half with different amounts of potassium hydroxide (pH > 7). HNO_3 and KOH were chosen since K^+ and NO_3^- ions are hardly adsorbed at the particle surface and do not modify the thickness of the ionic double layer. To our knowledge, isoelectric points of mixed spinel oxides from the Mn—Co—O ternary system have not yet been reported in the literature. We determined the electrophoretic mobilities and zeta potential values of the simple oxide Mn_3O_4. The latter value was calculated based on the former according to Smoluchovski's equation and Henry's function or Huckel's function [21]. The electrophoretic mobilities and zeta potential were very reproducible with error bars lower than 0.2 μm cm V^{-1} s^{-1} and 4 mV, respectively.

Particle granulometric distribution in colloidal dispersions was measured by Dynamic Light Scattering or DLS with a Zetasizer 3000 Malvern Instrument. In the case of a monodisperse distribution, the granulometric distribution is calculated by default using the cumulative method and indicated in percentage of intensity. The distribution in number is determined by Mie's theory from the intensity distribution. Each solution was diluted before DLS analysis but the pH and the salinity (or ionic strength) was the same as that for the concentrated original colloidal dispersion. In our study, three identical dilute dispersions were tested for each dispersion with an average of ten points for each dilute solution. A maximum uncertainty of ±5 nm was found over the whole range of measurements.

The rheological behavior of each colloidal dispersion was obtained for a spinel oxide solution concentration of 60 g L^{-1} with an Anton Parr MCR301 system by using a cone-plane type geometry (50 mm in diameter, 1° angle and 50 μm separator).

Optical transmittance and reflectance of oxide thin films deposited on 5 mm thick commercial glass substrates in the 300—1100 nm wavelength range were measured with a PV-300 from Bentham.

Topographic and roughness surface analyses were realized with a ZYGO instrument based on Mirau's interferometry and the Metropro software. This scanning white light interferometry technique provides a vertical scan range of up to 1 mm, and a lateral resolution of 0.5—1.2 microns (depending on the objective used × 40 or × 10, respectively).

3. Results & discussion

3.1. Influence of hydrodynamic parameters, physical and chemical properties for the precipitation of Mn_3O_4

A better understanding of the phenomena that control the synthesis of the nanoparticles with tailored size and morphology is important for their use as colloidal suspensions. The particle size strongly depends on the nucleation stage. Therefore, a study of the hydrodynamic conditions during the mixing of precursors and control of the physical and chemical characteristics of the environment (dilution, temperature, concentration, dielectric constant of the solution etc …) is essential to control the synthesis of oxide nanoparticles. This study first focused on Mn_3O_4 and then extended to a variety of manganese and cobalt spinel oxides in order to prove the large potential of this technique and to adjust the optical properties of nanomaterials based on composition.

For a precipitation initiated by the mixing of reactants, the way of mixing and speed are essential parameters. The nucleation stage, which is the first part of the precipitation, occurs at the reactants interfaces. A fast agitation induces a turbulent mode which is more efficient for the interaction of reactants and dispersion in the medium. The turbulent mode chosen here was maintained by a double blade mixer, with a diameter covering half of the beaker, and a constant speed of 300 rpm to avoiding bubbles that formed at higher speeds.

The precipitation of hydroxides and oxides is due to deprotonated water molecules coordinating to the hydrated cationic complex favored by the alkaline medium. A small pH variation is recommended in order to minimize the presence of heterogeneities. Therefore, we decided to introduce the salts in a much larger volume of the buffered alkaline solution. In order to ensure complete dissolution of the solid phase and to avoid heterogeneous nucleation the concentration of the precursor salt solution was fixed to 0.3 mol L^{-1}, which is around ten times larger than the salt solubility in distilled water at 20 °C. A stirring time of 30 min was chosen. During the aging period, a dissolution/reprecipitation phenomenon can occur, which is usually related to the precipitate solubility. This modifies the particle size and morphology with time. However, for very strong alkaline media just like in our precipitation environment (pH > 12), hardly any dissolution/precipitation phenomenon occurs. The condensed phases formed after introducing the metal salts solution in the alkaline medium are thus thermodynamically stable.

3.1.1. Alkaline solution dilution and supersaturation

The driving force of the precipitation is the supersaturation (S) as it is a crucial parameter for the particles crystal phase, size and shape. S can be determined in different ways, especially as a function of the species concentrations in solution or the chemical potentials related to the species activities. The latter is more relevant when the precipitation process involving the kinetics of product formation is very fast. The determination of S is complex with Mn_3O_4 as the cation presents two different oxidation states. The solution supersaturation in our system was calculated for the $Mn(OH)_2$ intermediate phase at 25 °C at three different volumes of alkaline solutions (150, 460 and 1400 mL) corresponding to concentrations of LiOH (C) equivalent to 0.419, 0.137 and 0.045 mol L^{-1}, respectively. At these conditions, S decreases from 6.6, 4.6 to 2.3 ($\times 10^8$), respectively. For high S values ($>10^3$) the nucleation rate increases and the growing stage is limited. SEM images and associated histograms (Fig. 1) show monodisperse preparations of oxides. Particle shape is identical but the average particle size decreases almost linearly with dilution. For C = 0.045 mol L^{-1}, the average particle size is 41 ± 12 nm. XRD patterns (Fig. 2) show that pure Mn_3O_4 is formed for each synthesis. As the alkaline solution concentration decreases, the average crystallite size, determined by the Debye-Scherrer formulae, decreases from 122 ± 59 to 30 ± 7 nm. So, when the dilution is increased, S and particle size both decrease. However, a lower S value should slow down the process of nucleation and favor the increase in the size of particles. A small variation in the very high S values, before and after dilution, will not influence the mechanisms of nucleation and growth, which are strongly related to the diffusion of the growing units. In conditions where S is high, the nucleation process is predominant and more homogeneous in the whole solution. Also, a dilute medium limits contacts between pre-existing nuclei and growing units which facilitates the generation of small particles.

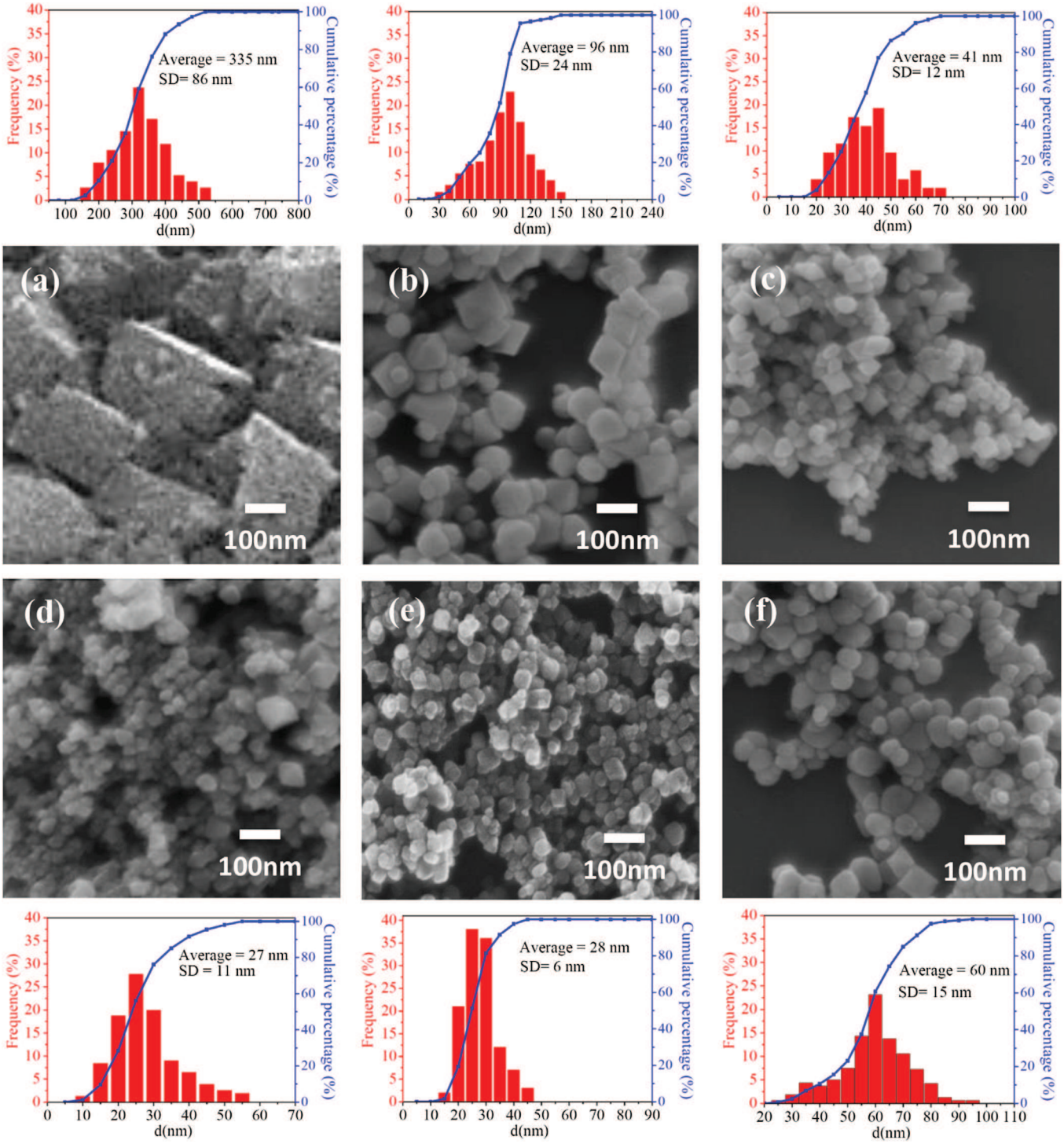

Fig. 1. SEM images and corresponding particle size distribution histograms for Mn_3O_4 after precipitation with (a) C_{LiOH} = 0.419 mol L^{-1}, (b) C_{LiOH} = 0.137 mol L^{-1}, (c) C_{LiOH} = 0.045 mol L^{-1} and fast introduction of metal salts at 25 °C; (d) for a buffered alkaline solution (C_{LiOH} = 0.045 mol L^{-1}) with a slow introduction of metal salts and (e) ~constant pH still at 25 °C; (f) fast introduction in LiOH (C_{LiOH} = 0.045 mol L^{-1}) at 50 °C.

3.1.2. Speed of reactants introduction and pH

According to Nielsen in 1964 [22], the uniform homogenization of the medium for a precipitation by a mixture of solutions is closely related to the type, speed and duration of mixing. The way the salt solution is introduced into the alkaline solution induces a variation in pH and modifies the contact points between reactants. We tested two extreme conditions of mixing: a slow introduction of the salt solution (drop by drop) with a constant debit over a period of time equivalent to 30 min, and a fast introduction (speed = 5.5 L s^{-1}) with the use of a large funnel. Note that the slow introduction of salt and the stirring period end at the same time. In this case, the pH varies almost linearly with time (Supplementary Information 1). For a fast introduction, the initial pH value of 12.2 decreases abruptly by one unit in a minute then tends to stabilize for the next 6 min before decreasing again to a pH value of 11.2 (reached after 400 s) which remains constant until the end of the

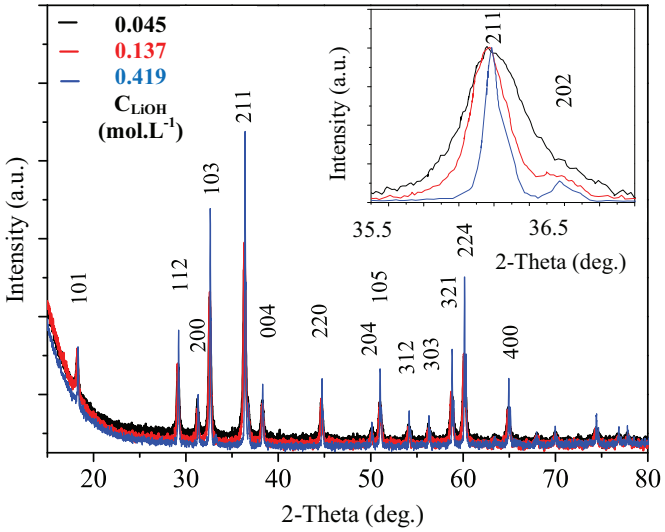

Fig. 2. XRD patterns of Mn_3O_4 after precipitation with (a) C_{LiOH} = 0.419 mol L^{-1}, (b) C_{LiOH} = 0.137 mol L^1, (c) C_{LiOH} = 0.045 mol L^{-1}. Inset shows (211) peak enlargement with the decrease of the alkaline solution concentration.

stirring sequence. Note that XRD analysis of the powder extracted from the solution after the first minute of fast introduction shows that crystallized Mn_3O_4 alone is observed therefore excluding a dissolution-reprecipitation process (see Supplementary Information 1). The final pH is identical in both cases. SEM images and associated histograms show that the only difference between the oxide particles obtained after each path of salt introduction into the alkaline solution is their average sizes, d = 27 ± 12 and 41 ± 12 nm for a slow and fast introduction, respectively (Fig. 1c and d). A similar crystallite size of 28 ± 7 nm is determined by the XRD patterns analysis of pure Mn_3O_4 obtained in both preparations. The slow introduction of a metal salt solution in an alkaline solution brings a constant amount of material without abrupt modification of the alkaline pH solution and creation of important heterogeneity zones. The nucleation process is therefore more homogeneous. However, a slow introduction can favor growth of particles. This is visibly hampered by the use of a very dilute medium. Knowing that an asymptote of the pH value is reached for a large amount of OH^- ions, we did the synthesis with a constant pH (pH ~ 12.3) for the whole mixing period by adding the salt solution to a large excess of LiOH powder (×1.6 the usual amount) dispersed in the same volume (1400 L) of alkaline solution. SEM images (Fig. 1c and e) and XRD patterns show that oxide nanoparticles crystallize as single crystals of similar shape and size (d = t = 28 ± 6 nm) compared to a slow introduction process (Supplementary Information 2).

3.1.3. Dielectric constant of the solvent

A change in the dielectric constant of the solvent used for preparing the alkaline solution can modify the number of nuclei and shape of particles created during the precipitation process [23]. The species solubility in the solution is directly related to the dielectric constant and will modify the S value. Experiments were carried out under our standard conditions with three different water/ethanol volume ratios: 100/0, 80/20 or 60/40. A comparison between SEM images shows that the average particle size decreases (d = 28, 26 and 20 ± 5 nm, respectively) when the dielectric constant of the medium decreases (Supplementary Information 3). This dielectric constant decreases from ~90 for pure distilled water to ~61 at 25 °C for a 60/40 volume ratio of water and ethanol. Crystallite sizes extracted from the full width at half maximum (FWHM) of pure Mn_3O_4 XRD patterns (Supplementary Information 4) using the Debye-Scherrer model are identical to the average particle sizes obtained from the SEM. The variation of the solution dielectric constant modifies the attractive forces between ions of opposite charges according to Coulomb's law. Ethanol gives a smaller dielectric constant than water. The use of ethanol decreases the solubility of the salt solution and the precipitating agent mixed together, which increases the medium supersaturation.

Also, the influence of the temperature on the synthesis was studied. The average particle size and distribution are larger at 50 °C than at room temperature (see Fig. 1e and Supplementary Information 5).

3.2. $Mn_{3-x}Co_xO_4$ ($0 < x < 3$) nanoparticles

Our synthesis method developed and optimized for Mn_3O_4 was applied to a larger range of compositions, with general formula $Mn_{3-x}Co_xO_4$ ($0 < x < 3$). $CoMn_2O_4$ and $MnCo_2O_4$ have already been prepared by soft chemistry methods [24]. This is the first study known to the authors on the complete Mn−Co−O spinel system synthesized at low temperature. The preparation of pure spinel oxides over a wide composition range is not straightforward. For instance, Aukrust and Muan's phase diagram shows the complexity of preparing pure manganese-rich spinel oxides at low temperature [25]. Such pure oxides can be obtained by usual solid state chemistry after quenching from high temperature or soft chemistry methods generally followed by thermal treatments. In the manganese and cobalt spinel oxide family, a structural transition is observed for a composition close to $Mn_{1.4}Co_{1.6}O_4$ at room temperature. In our case, stoichiometric amounts of metal salts were mixed together in water before pouring into the alkaline solution following our standard conditions. Five intermediate compositions were studied in detail, namely $Mn_{2.5}Co_{0.5}O_4$, $Mn_{2.0}Co_{1.0}O_4$, $Mn_{1.5}Co_{1.5}O_4$, $Mn_{1.0}Co_{2.0}O_4$ and $Mn_{0.5}Co_{2.5}O_4$. ICP-AES analyses confirmed the final mixed oxide compositions with a perfect stoichiometry match for each sample (within the 0.02 standard error of measurement). ICP-AES analyses also showed a very small concentration of Li^+ (lower than a few hundreds of ppm) and a maximum sulfur quantity of 0.3 wt% which remained after each sample precipitation. This proves the efficiency of our synthetic method and washing steps for the removal of most of the residual elements from each solution. XRD measurements were performed on each sample after precipitation (Fig. 3). Each single phase $Mn_{2.5}Co_{0.5}O_4$, $Mn_{2.0}Co_{1.0}O_4$ and $Mn_{1.5}Co_{1.5}O_4$ is tetragonal while $Mn_{1.0}Co_{2.0}O_4$ and $Mn_{0.5}Co_{2.5}O_4$ are cubic, in accordance with the literature [6]. Note that for the cobalt-rich spinel phases, the solution needs to be refluxed at 100 °C for up to 2 h (see Fig. 3b and c). The width and height of the (111) peak of the oxide phase indeed tend to indicate that a crystalline mixed oxy-hydroxyde phase is formed for Co-rich samples. The main intensity for the latter phase is observed at 21° in 2-Theta, which corresponds to the (003) reflection. This intermediate phase was also observed for the pure cobalt sample preparation [26]. This peak vanishes after refluxing for one and 2 h for $Mn_{1.0}Co_{2.0}O_4$ and $Mn_{0.5}Co_{2.5}O_4$, respectively, indicating that only the crystalline Co-rich spinel oxide phase is then present. Spinel oxide nanoparticles are spherical for all compositions and the average diameter progressively decreases from 38 ± 14 nm (for $Mn_{2.5}Co_{0.5}O_4$) to 23 ± 5 nm (for $Mn_{0.5}Co_{2.5}O_4$) with increasing cobalt. We performed neutron diffraction experiments on a Co-rich sample ($Mn_{1.0}Co_{2.0}O_4$) of cubic symmetry and a Mn-rich sample ($Mn_{2.0}Co_{1.0}O_4$) of tetragonal symmetry in order to determine their cation distributions (Fig. 4). Neutron diffraction can distinguish the manganese and cobalt elements due to distinct diffusion parameters. Rietveld refinements of the neutron data

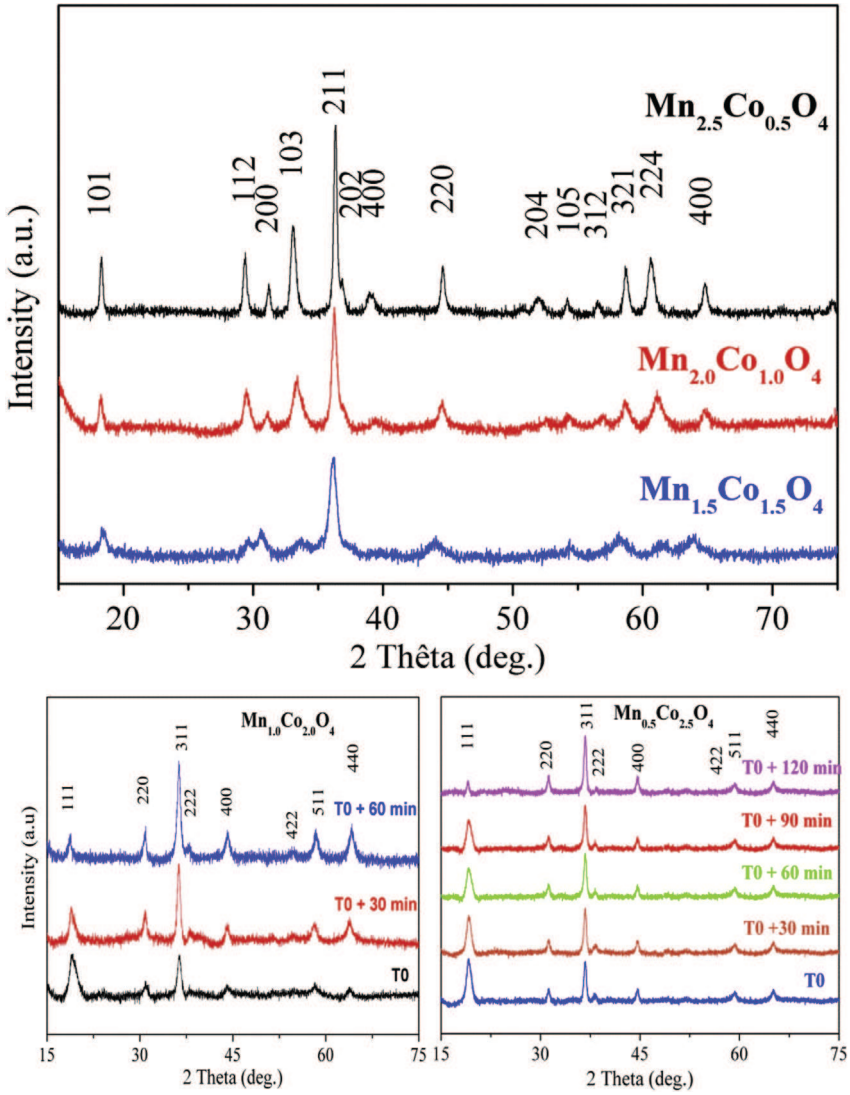

Fig. 3. XRD patterns of $Mn_{3-x}Co_xO_4$ with (top) tetragonal symmetry (x = 0.5, 1.0 and 1.5 from top to bottom) and (bottom) cubic symmetry after precipitation (T0) for (left) x = 2.0 and (right) x = 2.5. T0+ x min indicates the time of reflux at 100 °C after precipitation.

recorded at room temperature and the Bond Valence Sum (BVS) calculation indicate that the spinel oxide nanopowders contain mainly Co^{2+} on the tetrahedral site. Two couples of cations are determined on the octahedral site, for both phases, with a small quantity of Co^{3+} and Mn^{4+} for the Mn-rich phase. The cationic distributions can then be written as follows:

$$-Co^{2+}_{0.81}Mn^{2+}_{0.19}\left[Co^{2+}_{0.16}Co^{3+}_{0.03}Mn^{3+}_{1.76}Mn^{4+}_{0.06}\right]O_4, \quad \text{for } Mn_{2.0}Co_{1.0}O_4;$$

$$-Co^{2+}_{0.87}Mn^{2+}_{0.13}\left[Co^{2+}_{0.50}Co^{3+}_{0.63}Mn^{3+}_{0.44}Mn^{4+}_{0.43}\right]O_4, \quad \text{for } Mn_{1.0}Co_{2.0}O_4.$$

Similarly to the $MnCo_2O_4$ sintered ceramics, the cationic distribution as determined by the BVS calculations shows that our nanopowders of the same composition contain close concentrations of Co^{2+} and Co^{3+}, and Mn^{3+} and Mn^{4+}. Our previous study showed that a maximum of conductivity was obtained for a similar distribution, according to Verwey's law and the polaron hopping mechanism [6,24,27].

3.3. Colloidal dispersion stabilization of oxide nanoparticles

Many techniques such as electrophoresis, doctor blade, serigraphy, dip-coating or spin-coating were developed for the thin film

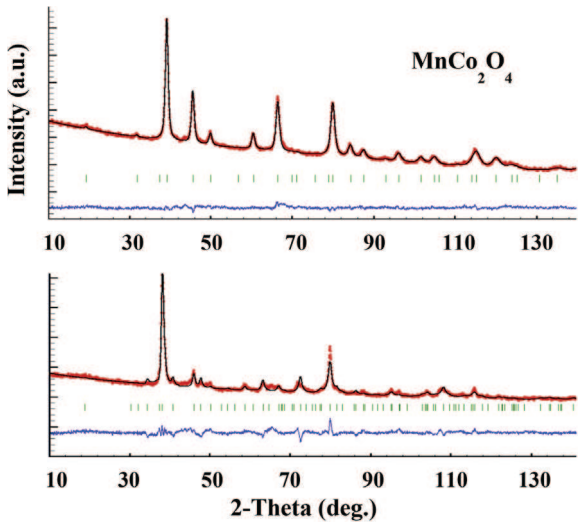

Fig. 4. Neutron diffraction patterns of (top) $MnCo_2O_4$ and (bottom) Mn_2CoO_4 nanopowders recorded on D2B, ILL ($\lambda = 1.594$ Å) after Rietveld refinements (observed = red dots, calculated = black lines, difference is in blue below). Reliability factors are: (top) $R_p = 0.174$, $R_{wp} = 0.121$, $R_{exp} = 0.088$, $\chi^2 = 1.89$, $R_B = 0.077$, $R_F = 0.056$ and (bottom) $R_p = 0.357$, $R_{wp} = 0.270$, $R_{exp} = 0.127$, $\chi^2 = 4.49$, $R_B = 0.120$, $R_F = 0.106$. (For interpretation of the references to color in this figure legend, the reader is referred to the web version of this article.)

preparation starting from a colloidal dispersion. Their advantages are numerous compared to the vapor deposition techniques: simple, low cost, no vacuum is required, possible extension to large surfaces etc … We chose the dip-coating technique for our thin film preparation. The quality of the thin layer, which can be evaluated by a homogeneous distribution of nanoparticles on the substrate, thickness, density and presence of cracks … is highly dependent on the physical and chemical properties of the colloidal dispersion (degree of particles dispersion, solvent volatility, sol viscosity, substrate wettability …).

After synthesis and centrifugation, the spinel oxide particles are maintained together as anionic flocculates by different attractive forces, mainly Van der Waals forces and surface tension at the liquid/particle interface. Ultrasonication at 35 kHz for 5 min was performed to break apart the agglomerates of particles in aqueous solution. Surface charges of oxides are due to the polarization of the oxygen electronic density by the metal which lowers the hydroxyl groups at the surface. Depending on the cation nature and oxidation state close to the oxide surface, differences in the type and number of hydroxyls groups are observed. Zetametry measurements were undertaken for each spinel oxide to determine their IsoElectric Points (IEP) and domains of colloidal dispersion stability (Fig. 5). The IEP values progressively increase with the cobalt content, varying from 7.0 for Mn_3O_4 to 10.5 for $Mn_{0.5}Co_{2.5}O_4$. These results indicate that the surface basicity of particles increase with the amount of cobalt. For all mixed spinel oxides, a large domain of constant zeta potential is observed for pH < 7. Zeta potential values of 40 ± 4 mV indicate a good stability of colloidal dispersions. A coloration of solution was observed for pH values lower than 6 due to partial dissolution of particles. Therefore, all preparations were peptized at pH = 6 with nitric acid and stabilized with an azeotrope mixture containing 96 vol.% of absolute ethanol and 4 vol.% of ultrapure water.

The granulometric distribution determined by the DLS method is given for each spinel oxide in Fig. 6. All solutions are monodisperse with a narrow particle size distribution. The hydrodynamic particle average diameter decreases when the cobalt content increases in the mixed spinel oxide, with a maximum of 148 nm for

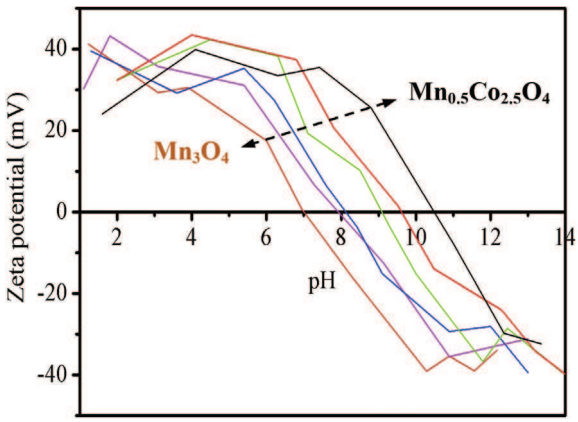

Fig. 5. Zeta potential variation with pH for $Mn_{3-x}Co_xO_4$ ($0 \leq x < 3$). Nitric acid was used for pH values <7 and potassium hydroxide for pH > 7.

Mn_3O_4 and 46 nm for $Mn_{0.5}Co_{2.5}O_4$.

Fig. 6 shows the viscosity variation as a function of the shear strain for each colloidal dispersion of spinel oxide. Two types of rheological behaviors can be identified: (i) for the Mn-rich phases with $x \leq 1.5$, which crystallize in the tetragonal structure, viscosity decreases with the constraints and a hysteresis is observed, indicating a rheofluidifying and thixotropic behavior while (ii) for the Co-rich phases of cubic symmetry with $x > 1.5$, viscosity remains constant over the whole measurement range which corresponds to a Newtonian behavior. Colloidal dispersions were stabilized for a few weeks up to six months and were used as such for the preparation of spinel oxide thin films at room temperature. A colloidal dispersion concentration of 60 g/L was chosen in order to obtain the thinnest possible homogeneous oxide layer on glass substrate (~300 nm). Note that this can also be achieved on quartz, metal and alloy substrates. Also, the azeotrope mixture containing essentially ethanol (96% in volume) allowed an excellent wettability of the substrate.

3.4. Spinel oxide thin films preparation by the dip-coating method and their optical properties

Oxide thin films of a thickness close to 300 nm were deposited with a NIMA DC small dip-coater from Lot-Oriel (withdrawal rate of 200 mm/min) on sodocalcic glasses (5 mm in thickness) which were preliminary cleaned with an alkaline detergent. FEG-SEM images show homogeneous layers and no cracks, although a better uniformity and compactness of the surface is noticed for the Co-rich phases, which contain smaller particles (Fig. 7). The surface profile of each oxide single layer was generated by white light optical interferometry measurements (see insets in Fig. 7). The 3D reconstructions show small uncovered entities on the substrate for the two manganese-rich phases Mn_3O_4 and $Mn_{2.5}Co_{0.5}O_4$ and the average arithmetic roughness is 0.23 ± 0.06 μm for both samples. In these small areas, the light goes straight through and is not reflected by the glass substrate, which generates dips in the surface profile. These dips are not present for higher cobalt concentrations and the surface is much more regular, homogeneous and compact with an arithmetic average of roughness surface of 0.012 ± 0.003. Single layer porosity is related to the physical and chemical properties of the dispersions, particularly to their stabilization by electrostatic repulsions. Particles rearrange to form a compact layer during the drying process. Xu and Anderson (1991) showed that the electrostatic repulsion forces were responsible for the film porosity [28]. The probability of particles to agglomerate increases with the

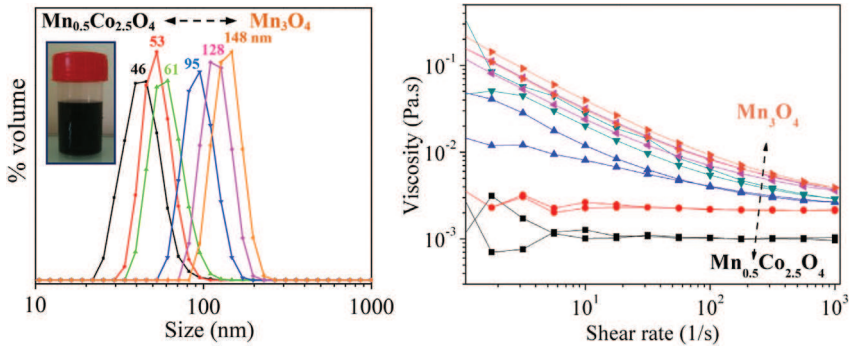

Fig. 6. (left) Percentage of intensity as a function of hydrodynamic particle diameter and (right) viscosity *vs* shearing stress for $Mn_{3-x}Co_xO_4$ ($0 \leq x < 3$).

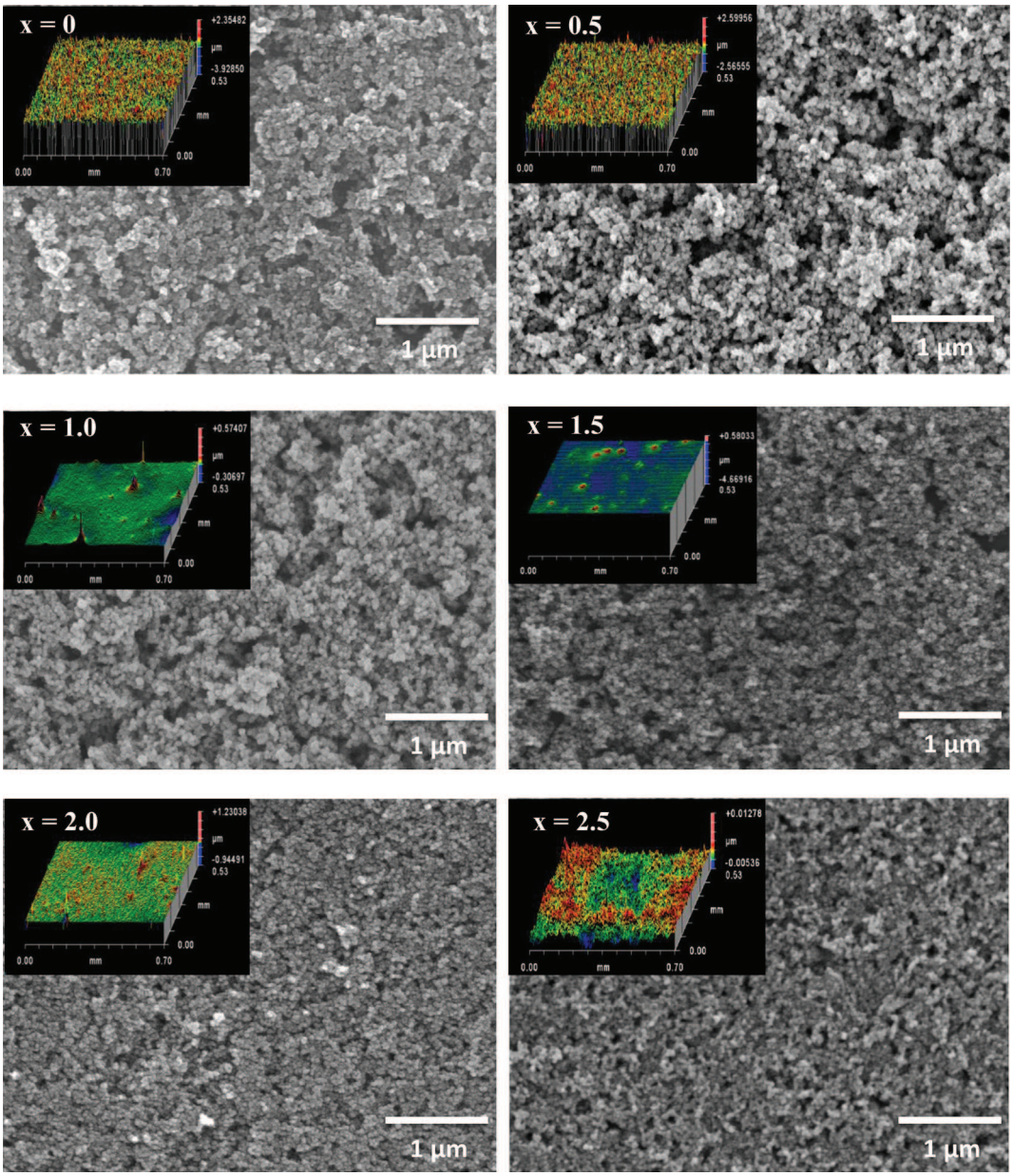

Fig. 7. FEG-SEM images and surface profiles (insets) of $Mn_{3-x}Co_xO_4$ ($0 \leq x < 3$) thin films prepared by dip-coating.

lowering of the particles repulsion energy. In our case, the average zeta potential decreases at pH = 6 when the cobalt content increases. During the retrieving stage of the substrate, the progressive solvent evaporation brings the particles closer to each other. For Mn-rich phases, minimizing the repulsive forces limits their reorganization and increases the film porosity.

The optical properties of all our spinel oxide thin films were determined at room temperature after subtracting the influence of the glass substrate. Transmittance (T) and reflectance (R) were measured from the UV region to the IR region, i.e. 300–1100 nm. The Absorbance (A) spectra were deduced from the transmittance and reflectance measurements by using the simplified relation: A = 1 − T − R (Fig. 8). Energy band gaps of spinel oxide semiconductors were determined by using Tauc's relation [29]. The best fit of $(\alpha h\upsilon)^x$ *vs* hυ curve plotted for each sample was for x = 2, which corresponds to a direct gap.

The absorbance spectrum for Mn_3O_4 shown in Fig. 8 is in accordance with the literature [30]. Three main areas can be isolated: (1) in the UV region, below 400 nm, where the absorbance is maximum (~98%) and fairly constant; (2) from 400 to 600 nm where the absorbance decreases abruptly and almost linearly down to ~17%; and (3) above 600 nm where the decrease in absorbance is slow until it becomes negligible in the IR region. The haussmanite cation distribution is usually described with a direct spinel structure as $Mn^{2+}[Mn^{3+}{}_2]O_4$, where Mn^{2+} ($3d^5$) is situated in the tetrahedral site with a high spin state configuration such as all five orbitals contain only one electron ($^2e\ ^3t_2$); the octahedral site is occupied by Mn^{3+} ($3d^4$) which exhibits a high spin state and ($^3t_{2g}\ ^1e_g$) configuration with a lifting of the e_g degenerated levels due to the Jahn-Teller effect. The insulating behavior usually observed in the direct spinel structure of Mn_3O_4 is not necessarily in contradiction with the low energy band gap between the valence band and conduction band which characterizes a semi-conductor. In the first case, the large resistivity of the spinel oxide is due to the isolation of one type of cation on each crystallographic site, which hampers the hopping of polarons (and thus the electronic conduction) otherwise observed when an element with two oxidation states (n and n + 1) are on the same type of crystallographic site, preferentially the octahedral sites due to shortest distances. In the second case, the energy levels related to the atomic orbitals as defined by the band theory, are reasonably separated (E_g < 3 eV) to create electron/hole pairs when under sufficient external energy, for instance heat or solar absorbance. The maximum absorbance observed in the UV region is generally attributed to a charge transfer between the oxygen p orbitals towards the d orbitals of the Mn^{2+} and Mn^{3+} cations [30,31]. Small intra-atomic d–d transitions between Mn^{3+} in octahedral crystal fields can occur at higher wavelengths and the interactions become negligible near the IR region. An optical direct band gap of 2.6 eV was determined for Mn_3O_4 (see Fig. 8), close to the value obtained by Xu et al., in 2006 (E_g = 2.54 eV) for Mn_3O_4 thin films prepared by chemical deposition in solution [32]. A gap of 2.36 eV was also determined on thin films of Mn_3O_4 but the authors attributed this lower value to the presence of a residual hydroxyl phase [33]. Inversely, a gap value of 3.3 eV was measured for spherical nanoparticles of Mn_3O_4 [34]. This gap shift towards higher energy values, associated with a blue shift, is due to a quantum confinement related to the small particle size and the separation of the continuous band into discrete levels. Such large optical band gaps are interesting for optoelectronic applications with light emission in the low wavelength regions. On the contrary, low gap values show an interesting aptitude of the material for solar absorbance as required for example in photocatalysis or photovoltaics.

The variations in the absorbance spectra for the mixed spinel oxide materials $Mn_{3-x}Co_xO_4$ (0 < x < 3) are similar to that of Mn_3O_4 with a general decrease of the absorbance with the increasing wavelength (see Fig. 8). However, the presence of cobalt in the spinel structure induces systematically a second absorption front near 700 nm in wavelength. This front is also observed in the end family member Co_3O_4 [35]. For stoichiometric Co_3O_4, the cation distribution is $Co^{2+}[Co^{3+}{}_2]O_4$, where Co^{2+} ions are positioned on the tetrahedral sites with a high spin state configuration $3d^7$ ($^3e\ ^4t_2$) while Co^{3+} ions occupy the octahedral sites with a low spin state configuration $3d^6$ ($^6t_{2g}\ ^0e_g$). A first absorption band in the UV region is attributed to the inter-atomic charge transfer from the anion to the cation, in the case of Co_3O_4, from the oxygen p orbitals to the d orbitals of both Co^{2+} and Co^{3+} [36]. The presence of the absorption edge at ~700 nm can be explained by the inter-atomic (cation–cation) charge transfer from the Co^{3+} d(t_{2g}) orbitals in octahedral sites to the Co^{2+} d(t_2) orbitals in tetrahedral sites [36,37]. Neutron diffraction measurements performed on our $MnCo_2O_4$ and $CoMn_2O_4$ samples provided evidence for both Co^{2+} and Co^{3+} on the two crystallographic sites of the spinel structure (see part 3.2). The absorption front measured in the visible region for all $Mn_{3-x}Co_xO_4$ (0 < x < 3) compounds could therefore be related to the inter-atomic Co^{3+} d(t_{2g}) to Co^{2+} d(t_2) transition. However, other inter-atomic transitions can also occur in the presence of Mn^{3+} and Mn^{4+}. Two band gaps are thus determined for each mixed oxide using Tauc's relation, associated to the two main peaks observed in the absorbance curve. Both band gaps decrease when the cobalt content increase (see Fig. 8). The highest band gap energy decreases from 2.6 eV for Mn_3O_4 down to 2.1 eV for $Mn_{0.5}Co_{2.5}O_4$. This is not due to the particle size and a quantum confinement effect since the Co-rich phase particles are the smallest while the haussmanite structural type material presents the largest particles. We believe that the decrease in the two energy gaps is directly related to the presence of lower empty d levels due to the presence of cobalt creating also an intermediate level in between the valence band and conduction band of the semiconducting materials, as previously reported [37]. Further investigations will be necessary in order to confirm this assumption. But the presence of an intermediate band in semi-conducting oxide materials that can be crystallized by a simple process at room temperature and deposited by a low-cost method as thin films will open very interesting opportunities for advances in electronics and optics.

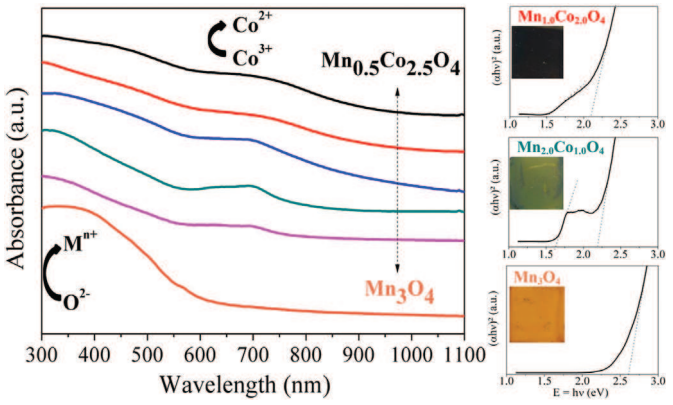

Fig. 8. Optical absorbance variation and $(\alpha h\upsilon)^2$ *vs* E = hυ curve for $Mn_{3-x}Co_xO_4$ ($0 \le x < 3$) thin films. Extrapolation of the straight lines near the edges in the $(\alpha h\upsilon)^2$ *vs* hυ curves gives energy band gaps of 2.60 for x = 0, 1.70 and 2.22 for x = 0.5, 1.62 and 2.18 for x = 1.0, 1.55 and 2.14 for x = 1.5, 1.48 and 2.13 for x = 2.0, and 1.43 and 2.08 for x = 2.5. *M* corresponds to the Metal cation.

4. Conclusions

The low-temperature sustainable synthesis and solution stabilization of functional nanoparticles was developed. This water and ethanol synthesis and solution stabilization of oxide nanoparticles was used to study a series of compounds with $Mn_{3-x}Co_xO_4$ ($0 \leq x < 3$) general formula.

Firstly, the main conditions that monitor the size and shape of the oxide nanoparticles directly crystallized at room temperature by precipitation were defined for Mn_3O_4. Increasing the alkaline solution (LiOH) concentration increases the supersaturation value and decreases particle sizes. Therefore, fast metal salt introduction into a much larger volume of a supersaturated and buffered alkaline solution rapidly stirred under turbulent conditions at room temperature can generate small oxide particles of isotropic shape. Mixed spinel oxides of manganese and cobalt were prepared using our standard conditions. For the Co-rich phases, a further reflux stage at 100 °C up to 2 h is required to obtain pure mixed spinel oxides. The cation distribution was determined for the $CoMn_2O_4$ tetragonal phase and $MnCo_2O_4$ cubic phase by neutron diffraction. In both cases, octahedral sites can contain four types of cations (Co^{2+}, Co^{3+}, Mn^{3+} and Mn^{4+}), while tetrahedral sites are mainly occupied by Co^{2+}, similarly to dense ceramics of the same compositions.

Secondly, the isoelectric points and pH stability domains were determined for all our solutions of oxide nanoparticles. The IEP value shifts from 7 for Mn_3O_4 to 10.5 for $Mn_{0.5}Co_{2.5}O_4$ and a large plateau of high zeta potential (40 ± 4 mV) in acidic conditions allowed the preparation of colloidal dispersions for a pH ~ 6. Monodisperse solutions in azeotropic medium (ethanol/water = 96/4 vol.%) were formed. The hydrodynamic particle diameter in such azeotropic medium decreases with the cobalt content. Mn-rich solutions are rheofluidifying and thixotropic while the cubic phases follow a Newtonian behavior.

Thirdly, spinel oxide thin films (~300 nm) were prepared by the dip-coating technique. These films exhibit strong solar absorbance at low wavelengths and then direct energy band gaps were determined. A second gap, which is observed systematically for Co-containing spinel oxide phases, was associated with the generation of an intermediate state in the optical band gap.

Recently, this method has been successfully extended to other families of spinel oxides including cuprates. In addition, our preliminary results indicate that the process can be adapted to synthesize ZnO, CuO, and Cu_2O, and has the potential to accommodate a wide range of target chemistries and stoichiometries and therefore, can constitute a promising method for enhanced efficiency in the preparation and use of nanomaterials containing critical elements. Moreover, since this innovative process does not require any organic reactant or polymeric agent, it is inherently low cost and can be easily adapted for large-scale production.

Acknowledgments

The French Ministry of Education and Research is thanked for financial assistance towards the salary of the PhD student. We also wish to thank Dr S.M. Moussa for her input. Dr Juan Claudio Nino from the NRG group at the University of Florida is deeply acknowledged for his interesting comments.

Appendix A. Supplementary data

Supplementary data related to this article can be found at http://dx.doi.org/10.1016/j.matchemphys.2015.05.065.

References

[1] S. Pal, D. Diso, S. Franza, A. Licciulli, L. Rizzo, Spectrally selective absorber coating from transition metal complex for efficient photothermal conversion, J. Mater. Sci. 48 (2013) 8268–8276.
[2] J. Vince, A. Šurca Vuk, U.O. Krašovec, B. Orel, M. Köhl, M. Heck, Solar absorber coatings based on $CoCuMnO_x$ spinels prepared via the sol–gel process: structural and optical properties, Sol. Energy Mater. Sol. Cells 79 (2003) 313–330.
[3] S.A. Eliziário, J.M. de Andrade, S.J.G. Lima, C.A. Paskocimas, L.E.B. Soledade, P. Hammer, Black and green pigments based on chromium–cobalt spinels, Mater. Chem. Phys. 129 (2011) 619–624.
[4] D. Visinescu, C. Paraschiv, A. Ianculescu, B. Jurca, B. Vasile, O. Carp, The environmentally benign synthesis of nanosized $Co_xZn_{1-x}Al_2O_4$ blue pigments, Dyes Pigm. 87 (2010) 125–131.
[5] K. Park, S.J. Kim, J.-G. Kim, S. Nahm, Structural and electrical properties of MgO-doped $Mn_{1.4}Ni_{1.2}Co_{0.4-x}Mg_xO_4$ ($0 \leq x \leq 0.25$) NTC thermistors, J. Eur. Ceram. Soc. 27 (2007) 2009–2016.
[6] H. Bordeneuve, A. Rousset, C. Tenailleau, S. Guillemet-Fritsch, Cation distribution in manganese cobaltite spinels $Co_{3-x}Mn_xO_4$ ($0 \leq x \leq 1$) determined by thermal analysis, J. Therm. Anal. Calorim. 101 (2009) 137–142.
[7] S. Royer, D. Duprez, Catalytic oxidation of carbon monoxide over transition metal oxides, ChemCatChem. 3 (2011) 24–65.
[8] S. Rühle, A.Y. Anderson, H.-N. Barad, B. Kupfer, Y. Bouhadana, E. Rosh-Hodesh, A. Zaban, All-oxide photovoltaics, J. Phys. Chem. Lett. 3 (2012) 3755–3764.
[9] Y.S. Jung, J.Y. Seo, D.W. Lee, D.Y. Jeon, Influence of DC magnetron sputtering parameters on the properties of amorphous indium zinc oxide thin film, Thin Solid Films 445 (2003) 63–71.
[10] L. Miao, P. Jin, K. Kaneko, a Terai, N. Nabatova-Gabain, S. Tanemura, Preparation and characterization of polycrystalline anatase and rutile TiO_2 thin films by rf magnetron sputtering, Appl. Surf. Sci. 212–213 (2003) 255–263.
[11] T. Maruyama, Copper oxide thin films prepared by chemical vapor deposition from copper dipivaloylmethanate, Sol. Energy Mater. Sol. Cells 56 (1998) 85–92.
[12] N. Bahlawane, E. Fischer Rivera, K. Kohse-Höinghaus, A. Brechling, U. Kleineberg, Characterization and tests of planar Co_3O_4 model catalysts prepared by chemical vapor deposition, Appl. Catal. B Environ. 53 (2004) 245–255.
[13] T. Pauporté, D. Lincot, Electrodeposition of semiconductors for optoelectronic devices: results on zinc oxide, Electrochim. Acta 45 (2000) 3345–3353.
[14] M. Wu, Y. Huang, C. Yang, J. Jow, Electrodeposition of nanoporous nickel oxide film for electrochemical capacitors, Int. J. Hydrogen Energy 32 (2007) 4153–4159.
[15] R.N. Singh, J.P. Pandey, N.K. Singh, B. Lal, P. Chartier, J.-F. Koenig, Sol–gel derived spinel $M_xCo_{3-x}O_4$ ($M = Ni, Cu$; $0 \leq x \leq 1$) films and oxygen evolution, Electrochim. Acta 45 (2000) 1911–1919.
[16] A. Phani, M. Passacantando, S. Santucci, Synthesis and characterization of zinc aluminum oxide thin films by sol–gel technique, Mater. Chem. Phys. 68 (2001) 66–71.
[17] X. Zhao, Q. Zhao, J. Yu, B. Liu, Development of multifunctional photoactive self-cleaning glasses, J. Non. Cryst. Solids 354 (2008) 1424–1430.
[18] J. Rodríguez-Carvajal, FULLPROF: a program for rietveld refinement and pattern matching analysis, in: Satell. Meet. Powder Diffr. XV IUCr Congr, 1990, p. 127.
[19] I.D. Brown, D. Altermatt, Bond-valence parameters obtained from a systematic analysis of the inorganic crystal structure database, Acta Crystallogr. Sect. B 41 (1985) 244–247.
[20] M.R. Wood, G.J. Palenik, Bond valence sums in coordination chemistry. A simple method for calculating the oxidation state of cobalt in complexes containing only Co–O bonds, Inorg. Chem. 37 (1998) 4149–4151.
[21] H. Ohshima, Henry's function for electrophoresis of a cylindrical colloidal particle, J. Colloid Interface Sci. 180 (1996) 299–301.
[22] A.E. Nielsen, Kinetics of Precipitation, Pergamon, Oxford, 1964.
[23] G. Charlot, B. Tremillon, Chemical Reactions in Solvents and Melts, Translated from the French edition (Paris, 1963) by P. J. J. Harvey, Pergamon, New York, 1969.
[24] G. Salek, S. Guillemet-Fritsch, P. Dufour, C. Tenailleau, A simple preparation process of pure $Mn_{3-X}Co_xO_4$ ($X = 1, 1.5$ and 2) desert rose-like nanoparticles and their optical properties, Int. J. Chem. 4 (2012) 44–53.
[25] E. Aukrust, A. Muan, Phase relations in the system cobalt oxide-manganese oxide in air, Trans. Metall. Soc. Aime 230 (1964) 378–382.
[26] G. Salek, P. Alphonse, P. Dufour, S. Guillemet-Fritsch, C. Tenailleau, Low-temperature carbon monoxide and propane total oxidation by nanocrystalline cobalt oxides, Appl. Catal. B Environ. 147 (2014) 1–7.
[27] E.J.W. Verwey, P.W. Haaijman, F.C. Romeijn, G.W. Van Oosterhout, Controlled-valency semiconductors, Philips Res. Rep 5 (1950) 173–187.
[28] Q. Xu, M.A. Anderson, Synthesis of porosity controlled ceramic menbranes, J. Mater. Res. 6 (1991) 1073–1081.
[29] J. Tauc, Optical properties and electronic structure of amorphous, Mater. Res. Bull. 3 (1968) 37–46.
[30] V. Sanchez, Influence of tile synthesis parameters on the structural and textural properties of precipitated manganese oxides 3 (2001) 889–899.
[31] A. Vázquez-Olmos, R. Redón, A.L. Fernández-Osorio, J.M. Saniger, Room-temperature synthesis of Mn_3O_4 nanorods, Appl. Phys. A 81 (2005)

1131–1134.
[32] H.Y. Xu, S. Le Xu, X.D. Li, H. Wang, H. Yan, Chemical bath deposition of hausmannite Mn_3O_4 thin films, Appl. Surf. Sci. 252 (2006) 4091–4096.
[33] D.P. Dubal, D.S. Dhawale, R.R. Salunkhe, S.M. Pawar, C.D. Lokhande, A novel chemical synthesis and characterization of Mn_3O_4 thin films for super-capacitor application, Appl. Surf. Sci. 256 (2010) 4411–4416.
[34] N.M. Hosny, a. Dahshan, Facile synthesis and optical band gap calculation of Mn_3O_4 nanoparticles, Mater. Chem. Phys. 137 (2012) 637–643.
[35] K. Kolipaka, V. Brueser, A. Quade, J. Schaefer, Structural and Optical Characterization of Spinel Type Cobalt Oxide Nanoparticles Embedded in Amorphous Silicon Oxide Matrix Prepared by a Hybrid PVD/PECVD, 2011, pp. 2–5. Ispc-Conference.org.
[36] P.Y. Keng, B.Y. Kim, I. Shim, R. Sahoo, P.E. Veneman, N.R. Armstrong, et al., Colloidal polymerization of polymer- into cobalt oxide nanowires 3 (2009) 3143–3157.
[37] S. Thota, A. Kumar, J. Kumar, Optical, electrical and magnetic properties of Co_3O_4 nanocrystallites obtained by thermal decomposition of sol–gel derived oxalates, Mater. Sci. Eng. B 164 (2009) 30–37.